5.1 A NEW THEORY FOR THE ATMOSPHERIC ENERGY SPECTRUM

Ross Tulloch and K. Shafer Smith*
Center for Atmosphere Ocean Science
Courant Institute of Mathematical Sciences
New York University

1. INTRODUCTION

The horizontal kinetic and potential energy spectra of the atmosphere near the tropopause, observed during the Global Atmospheric Sampling Program (GASP) in the 1970's and analyzed by Nastrom and Gage (1985), have a steep -3 spectral slope on synoptic scales ($\approx$ 3,000km-1,000km) followed by a smooth transition to a shallow $-5/3$ spectral slope on the mesoscales ($\approx$ 500km-10km). The synoptic scale -3 slope is consistent with the forward potential enstrophy cascade expected in geostrophic turbulence, but geostrophic scaling should continue to hold near and below 500km, where the transition to $-5/3$ is observed to occur. Attempts to explain the observed shallowing transition in the spectra are so far incomplete.

Analysis of horizontal velocity data collected during the Pacific Exploratory Mission at altitudes between 9 and 12km over the Pacific Ocean indicate that mesoscale energy is dominated by vortical modes rather than divergent modes (Cho et al., 1999) and that the $-5/3$ slope is due to a forward energy cascade at scales smaller than 100km (Cho and Lindborg, 2001). Thus it is unlikely that the -5/3 part of the spectra is due to either a two dimensional inverse cascade or to gravity wave production by divergent flows.

The ideas of geostrophic turbulence (Charney, 1971) that lead one to expect only an inverse cascade of energy in balanced dynamics explicitly neglect surface dynamics. Surface quasigeostrophic (SQG) flow, proposed by Blumen (1978) as a counterpoint to geostrophic turbulence, is the special case of quasigeostrophic (QG) dynamics with uniform potential vorticity and non-uniform potential temperature on the boundaries. In SQG the total energy of the three-dimensional system and the available potential energy (APE) on the boundaries are separately conserved. This results in an inverse cascade of total 3D energy, but a forward cascade of boundary APE, with a $-5/3$ spectral slope. Because surface kinetic energy in SQG is related to the surface APE by a constant, the kinetic energy at the boundary also exhibits a $-5/3$ spectrum.

The relevance of SQG to atmospheric dynamics was considered by Blumen (1978), Juckes (1994), Held et al. (1995) and Hakim et al. (2002). Tulloch and Smith (2006) considered a depth limited SQG flow with constant stratification N, rigid lid, an isothermal lower boundary and random large-scale forcing. The kinetic energy spectrum for the inertial range of this system is

$$\mathcal{E}(K) = C_T \epsilon^{2/3} [\tanh(K/k_d)]^{-4/3} K^{-5/3} \tag{1}$$

which transitions from a -3 to a $-5/3$ slope at wavenumber $k_d = f/(NH)$ for a fluid of depth H, where ϵ is the flux of boundary energy. Unfortunately, the transition scale k_t is near the scale of Eady baroclinic instability so it is unlikely that the -3 part of the cascade would appear with baroclinic forcing. Moreover, taking the tropopause height to be about H = 10km results in an expected transition scale that is about ten times larger than the observed transition scale Nastrom and Gage (1985).

Much of the inadequacy of the finite-depth SQG model results because potential vorticity dynamics are suppressed, and the forcing is artificial. Here we include interior dynamics and baroclinic forcing by mean zonal shear. This model creates a large-scale interior-dominated forward potential enstrophy cascade (with spectral slope -3) which transitions to a surface-dominated surface energy cascade at small scales (with spectral slope $-5/3$). A bottom surface is included to dissipate large-scale energy through Ekman friction. This scenario should result in energy equipartition between kinetic and potential energy in both regimes of the cascade since the -3 large scale regime should obey the Charney (1971) theory. Moreover the transition wavenumber k_t in this model will depend on the relative strengths of interior and boundary mean gradients, rather than on the depth of the fluid.

2. SURFACE-INTERIOR INTERACTION MODEL

We assume mean baroclinic wind $\boldsymbol{U}(z)$ and potential vorticity $Q(z)$ that depend only on the vertical coordinate, and an eddy potential vorticity $q(x, y, z, t)$. The evolution equation is

$$q_t + J(\psi, q) = -\boldsymbol{U} \cdot \nabla q - \boldsymbol{u} \cdot \nabla Q, \tag{2}$$

where $\boldsymbol{u} = u\hat{\boldsymbol{x}} + v\hat{\boldsymbol{y}} = -\psi_y\hat{\boldsymbol{x}} + \psi_x\hat{\boldsymbol{y}}$, with ψ the streamfunction, ∇ is a horizontal gradient, and $J(A, B) = A_x B_y - A_y B_x$ is the Jacobian operator. The potential vorticity is related to the streamfunction by

$$q = \nabla^2\psi + \Gamma\psi, \tag{3}$$

where

$$\Gamma \equiv \partial_z \frac{f^2}{N^2} \partial_z \tag{4}$$

is the vortex stretching operator, f is the Coriolis frequency, $N^2 = (g/\theta_0) d\Theta/dz$ is the mean stratification, and

*Corresponding author address: K. Shafer Smith, Center for Atmosphere Ocean Science, New York University, 251 Mercer Street, New York, NY 10012. E-mail: shafer@cims.nyu.edu

z is a pseudo height. Similarly, the mean potential vorticity is related to the mean wind and meridional gradient of the Coriolis frequency β by

$$\nabla Q = \Gamma V \hat{\boldsymbol{x}} + [\beta - \Gamma U]\,\hat{\boldsymbol{y}}. \tag{5}$$

In our model we assume a doubly periodic domain in the horizontal and rigid boundaries at the top and bottom surfaces. We also allow for dissipation by Ekman friction at the lower surface, so our boundary conditions for potential temperature at the top θ^T and bottom θ^B are

$$\theta^T_t + J(\psi(z_T), \theta^T) = -\boldsymbol{U}(z_T)\cdot\nabla\theta^T - \boldsymbol{u}(z_T)\cdot\nabla\Theta^T, \tag{6}$$

$$\theta^B_t + J(\psi(z_B), \theta^B) = -\boldsymbol{U}(z_B)\cdot\nabla\theta^B - \boldsymbol{u}(z_B)\cdot\nabla\Theta^B - r\nabla^2\psi(z_B), \tag{7}$$

where r is the Ekman drag coefficient, and the mean potential temperature gradients $\nabla\Theta^{T,B}$ in thermal wind balance with the mean winds

$$\frac{g}{\theta_0}\nabla\Theta^{T,B} = f\left(V^{T,B}_z\hat{\boldsymbol{x}} - U^{T,B}_z\hat{\boldsymbol{y}}\right). \tag{8}$$

Finally, the potential temperature at the boundaries is related to the streamfunction by Neumann boundary conditions

$$f\left.\frac{\partial\psi}{\partial z}\right|_{z=z_T,z_B} = \frac{g}{\theta_0}\theta^{T,B}, \tag{9}$$

so that initial fields θ^T, θ^B, and q can be inverted for the streamfunction, from which the flow field can be diagnosed.

Since the problem of inverting potential vorticity in (3) with boundary conditions (9) is linear we can decompose the total streamfunction into an interior component and surface components $\psi = \psi^I + \psi^T + \psi^B$ (Lapeyre and Klein, 2006), where $\psi^I(x, y, z, t)$ solves the interior problem

$$\nabla^2\psi^I + \Gamma\psi^I = q, \qquad \left.\psi^I_z\right|_{z=z_T} = 0, \qquad \left.\psi^I_z\right|_{z=z_B} = 0, \tag{10}$$

and $\psi^T(x, y, z, t)$ and $\psi^B(x, y, z, t)$ solve the surface problems

$$\nabla^2\psi^T + \Gamma\psi^T = 0, \quad \left.f\psi^T_z\right|_{z=z_T} = \frac{g}{\theta_0}\theta^T, \quad \left.\psi^T_z\right|_{z=z_B} = 0, \tag{11}$$

$$\nabla^2\psi^B + \Gamma\psi^B = 0, \quad \left.\psi^B_z\right|_{z=z_T} = 0, \quad \left.f\psi^B_z\right|_{z=z_B} = \frac{g}{\theta_0}\theta^B. \tag{12}$$

When we let the horizontal domain be doubly periodic, the solution to equation (10) can be written as a sum of horizontal Fourier components and vertical modes of the associated Sturm-Liouville problem

$$\psi^I(x, y, z, t) = \sum_{\boldsymbol{K}}\sum_{m\geq 0}\tilde{\psi}_m(\boldsymbol{K}, t)\phi_m(z)e^{i\boldsymbol{K}\cdot\boldsymbol{x}}, \tag{13}$$

where $\boldsymbol{K} = (k_x, k_y)$ is the wavenumber vector and ϕ_m are the eigenfunctions which solve

$$\Gamma\phi_m = -\lambda^2_m\phi_m, \quad \left.\frac{d}{dz}\phi_m\right|_{z=z_T} = 0, \quad \left.\frac{d}{dz}\phi_m\right|_{z=z_B} = 0. \tag{14}$$

Similarly we can write the solutions of (11) and (12) as

$$\psi^{T,B}(x, y, z, t) = \sum_{\boldsymbol{K}}\tilde{\psi}^{T,B}(\boldsymbol{K}, t)\phi^{T,B}(K, z)e^{i\boldsymbol{K}\cdot\boldsymbol{x}}, \tag{15}$$

where $K = |\boldsymbol{K}|$.

The interior and surface modes can be obtained numerically for arbitrary stratification, but here we specialize to constant stratification N. Taking $z_T = 0$ and $z_B = -H$, the surface modes are

$$\phi^T = \frac{\cosh[KN(z+H)/f]}{\cosh(KNH/f)}, \quad \phi^B = \frac{\cosh(KNz/f)}{\cosh(KNH/f)} \tag{16}$$

and the interior modes are

$$\phi_m = \sqrt{2}\cos(m\pi z/H), \quad \lambda_m = \frac{m\pi f}{NH}. \tag{17}$$

In this case the inversion between the advected variables and the streamfunction takes on the simple form

$$q(x, y, z, t) = -\sum_{\boldsymbol{K}}\sum_{m\geq 0}(K^2 + \lambda^2_m)\phi_m(z)\tilde{\psi}_m(\boldsymbol{K}, t)e^{i\boldsymbol{K}\cdot\boldsymbol{x}} \tag{18}$$

$$\theta^T(x, y, t) = \sum_{\boldsymbol{K}}\frac{\theta_0 KN}{g}\tanh(KNH/f)\tilde{\psi}^T(\boldsymbol{K}, t)e^{i\boldsymbol{K}\cdot\boldsymbol{x}} \tag{19}$$

$$\theta^B(x, y, t) = -\sum_{\boldsymbol{K}}\frac{\theta_0 KN}{g}\tanh(KNH/f)\tilde{\psi}^B(\boldsymbol{K}, t)e^{i\boldsymbol{K}\cdot\boldsymbol{x}}. \tag{20}$$

Because the interior modes $\phi_n(z)$ are orthonormal, one can find the advection equation for the n-th mode of potential vorticity by expanding variables in modes, multiplying (2) by ϕ_n and integrating vertically (here we write the general form applicable for arbitrary N)

$$\begin{aligned}
&\frac{1}{H}\int_{-H}^{0}\phi_n(z)\left(q_t + J(\psi, q) + \boldsymbol{U}\cdot\nabla q + \boldsymbol{u}\cdot\nabla Q\right)dz = 0\\
&\Rightarrow \frac{\partial}{\partial t}\tilde{q}_n + \sum_{\ell m}\varepsilon_{\ell mn}\hat{J}(\tilde{\psi}_\ell, \tilde{q}_m) + \sum_m\hat{J}(\gamma^T_{mn}\tilde{\psi}^T + \gamma^B_{mn}\tilde{\psi}^B, \tilde{q}_m) =\\
&\qquad -ik\sum_{\ell m}\varepsilon_{\ell mn}\left(\tilde{U}_m\lambda^2_m\tilde{\psi}_\ell + \tilde{U}_\ell\tilde{q}_m\right)\\
&\qquad -ik\sum_m\left[\tilde{U}_m\lambda^2_m\left(\gamma^T_{mn}\tilde{\psi}^T + \gamma^B_{mn}\tilde{\psi}^B\right) + \xi_{mn}\tilde{q}_m\right]\\
&\qquad -ik(\beta - \Gamma U^s)\left(\tilde{\psi}_n + \alpha^T_n\tilde{\psi}^T + \alpha^B_n\tilde{\psi}^B\right),
\end{aligned} \tag{21}$$

where $\hat{J}$ symbolically denotes the summation over horizontal wavenumbers and ΓU^s is the constant mean meridional gradient of the vortex stretching term due to surface gradients. The coefficients

$$\begin{aligned}
\varepsilon_{\ell mn} &= \frac{1}{H}\int_{-H}^{0}\phi_\ell\phi_m\phi_n dz,\\
\alpha^{T,B}_n &= \frac{1}{H}\int_{-H}^{0}\phi_n\phi^{T,B}dz,\\
\gamma^{T,B}_{mn} &= \frac{1}{H}\int_{-H}^{0}\phi_m\phi_n\phi^{T,B}dz,\\
\xi_{mn} &= \frac{1}{H}\int_{-H}^{0}\phi_m\phi_n U^s(z)dz.
\end{aligned} \tag{22}$$

represent self interaction of the internal modes, and interactions between the interior and surfaces.

The conserved energy in the system is obtained by multiplying the potential voriticty by minus the full streamfunction and integrating over the depth. In Fourier space the energy is

$$E = \frac{1}{2}H\Re\sum_{\boldsymbol{K}}\sum_{m\geq 0}\left(K^2+\lambda_m^2\right)\tilde{\psi}_m^2 + \frac{1}{2}\frac{f}{N^2}\frac{g}{\theta_0}\Re\sum_{\boldsymbol{K}}\left(\tilde{\psi}^{T*}\hat{\theta}^T - \tilde{\psi}^{B*}\hat{\theta}^B + 2\frac{\tilde{\psi}^B\hat{\theta}^T}{\cosh(KNH/f)}\right) + \frac{f}{N^2}\frac{g}{\theta_0}\Re\sum_{\boldsymbol{K}}\sum_{m\geq 0}\left(\phi_m(0)\tilde{\psi}_m^*\hat{\theta}^T - \phi_m(-H)\tilde{\psi}_m^*\hat{\theta}^B\right) \quad (23)$$

where $\lambda_m = m\pi f/(NH)$ are the eigenvalues of (14), hats $\hat{}$ denote Fourier transformed variables, and * denotes the complex conjugate. The first three terms in (23) are the interior energy and the two surface energies, while the last three terms are the interactions between the two surfaces and the interactions between the interior modes and each surface.

3. NUMERICAL SIMULATIONS WITH A TRUNCATED MODEL

We derive a truncated model (termed the 2S2M model) by making the following assumptions: (1) constant N, (2) a truncation of the interior expansion to just two modes (barotropic and baroclinic), and (3) a mean flow that is decomposed into interior and surface parts, with the interior part projecting only onto the baroclinic mode ($\tilde{U}_0 = 0$, $\tilde{U}_1 \neq 0$). With constant stratification, the coefficients (22) can be computed analytically. Equation (21) becomes four advection equations: one for each surface, and one for each remaining internal mode. Note that each field is advected by the full streamfunction, with contributions from both the surfaces and interior modes at each level.

A series of simulations with the 2S2M model were computed, varying the strength of the top surface temperature gradient $\Theta_y^T = -2, -1, -0.5, -0.25$, while holding constant the mean interior wind $U^I = (4/\pi)\cos(\pi z/H)$ (*i.e.,* $\tilde{U}_1 = 2\sqrt{2}/\pi$) and setting the bottom gradient to zero ($-\Theta_y^B = 0$). A small deformation wavenumber $k_d = L/(2\pi)f/(NH) = 2$ was used in order to have as large a forward cascade range as possible. The relative Coriolis gradient is $\check{\beta} = \beta(\Delta U)^{-1}k_d^{-2} = 1$, where $\Delta U = \sqrt{2}\pi\tilde{U}_1 - (\Theta_y^T + \Theta_y^B)/2$ is the nondimensional velocity that scales with the linear growthrate. The relative Ekman drag $\check{r} = r(\Delta U)^{-2}k_d^{-1} = 0.02$ is small to minimize its effects on small scales. The forward cascade is dissipated with a scale-selective exponential cutoff filter that affects a narrow range of wavenumbers close to $k_{\max}$ (the largest resolved horizontal wavenumber).

Figure 1 shows the components that make up the kinetic energy spectra at the top surface in the case with $\Theta_y^T = -0.5$ and a horizontal resolution of 2048^2. The kinetic energy spectrum at the top surface, $K^2\hat{\psi}(z=0)^2$, is dominated by the -3 sloped barotropic kinetic energy spectrum, $K^2\tilde{\psi}_0^2$, at large scales and transitions to the $-5/3$ slope of the temperature variance, $(g\hat{\theta}^T/N\theta_0)^2$ at small scales.

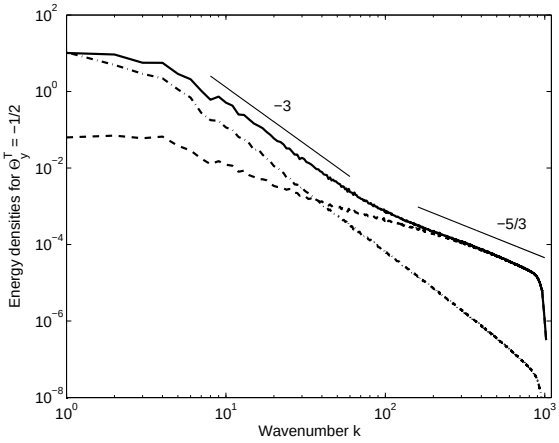

FIG. 1: Energy densities as a function of horizontal wavenumber $K = |\boldsymbol{K}|$ for the simulation with $\Theta_y^T = -.5$. Kinetic energy density at the top surface (solid line), barotropic kinetic energy (dash-dot), and variance of potential temperature (dashed).

The flux of available potential energy at the top surface

$$\epsilon(K) = \frac{g^2}{\theta_0^2 N^2}\sum_1^K \hat{\theta}^T\hat{J}(\hat{\psi}(z=0),\hat{\theta}^T) \quad (24)$$

is approximately constant over the $-5/3$ range ($\epsilon \approx 0.24$ nondimensionally) as shown in Figure 2. If we then

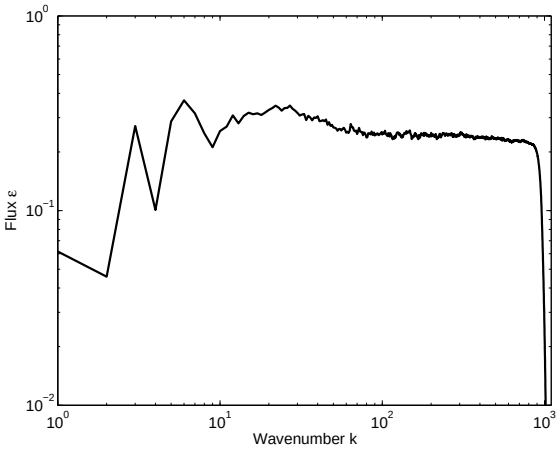

FIG. 2: Flux of available potential energy at the top surface for the simulation with $\Theta_y^T = -0.5$.

take this energy flux and the surface spectrum in figure 1 and compare them with Kolmogorov scaling $\mathcal{E}(k) = C\epsilon^{2/3}k^{-5/3}$, we find $C \approx 3.9$.

Figures 3 and 4 show that the transition scale is independent of resolution and dependent on the relative strength of the interior and surface forcings. In figure 4 the relative strength of the surface forcing is var-

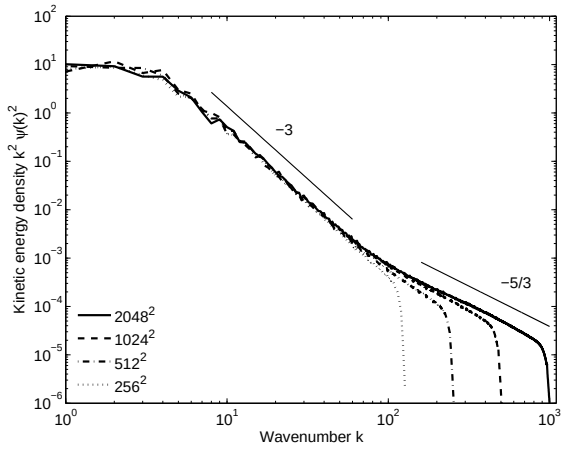

FIG. 3: Kinetic energy spectra at $z = 0$ with $\Theta_y^T = -.5$ computed for different horizontal resolutions.

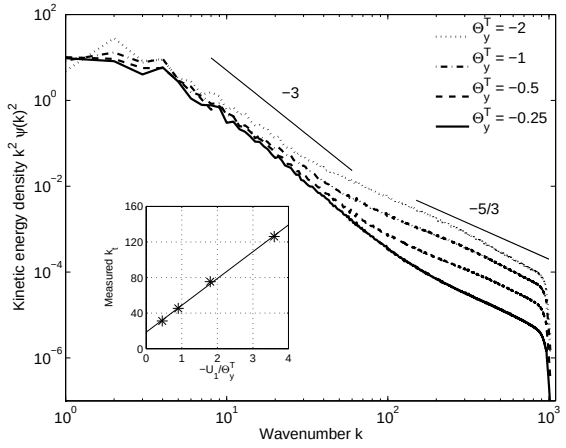

FIG. 4: Kinetic energy spectra at $z = 0$ with $\Theta_y^T = -2$, -1, -0.5, and -0.25 and $\tilde{U}_1 = 2\sqrt{2}/\pi$. (Inset) The measured transition wavenumber, defined as where the slope is $k^{-7/3}$, compared with the ratio $-\tilde{U}_1/\Theta_y^T$.

ied as all other parameters, including the interior forcing, are held constant. The linear growthrates for these simulations (not shown) are nearly the same, peaking at zonal wavenumber $K \approx 2k_d$ with growthrate $\omega_i \approx 0.15(\Delta U)f/(NH)$ and longwave cutoff due to β at zonal wavenumber $K \approx 1.5k_d$. The inset shows that the transition wavenumber varies linearly with $\tilde{U}_1/\Theta_y^T$.

Figure 5 shows that the transition to a $-5/3$ slope occurs only near the boundary since the SQG surface modes (16) decay exponentially with height when $K > k_d$. The kinetic energy at middepth $z = -H/2$ is mainly barotropic with minimal surface influence, and the SQG dynamics at the bottom are unforced and damped by the Ekman drag.

Finally, we ran a simulation with realistic atmospheric

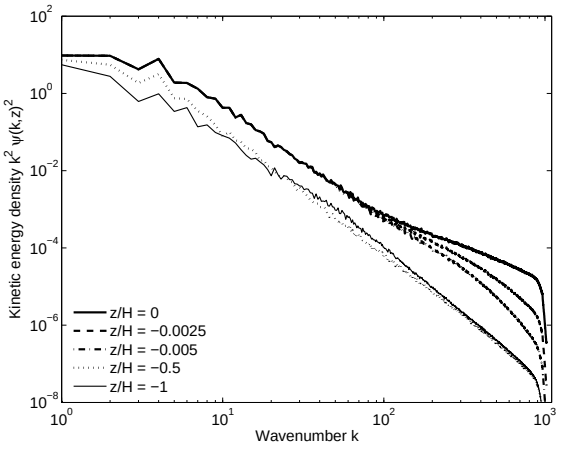

FIG. 5: Kinetic energy spectra at different height values with $\Theta_y^T = -0.5$.

forcing to verify that SQG dynamics emerge at small scales at the upper boundary in our model. Using NCEP long term monthly mean data, a mean wind profile is computed by averaging temporally, zonally and from 30°N to 60°N (where most of the GASP data is from). The meridional potential temperature gradients from the 1000 mb and 200 mb data are computed by differencing the 60°N and 30°N averages, from which the mean zonal wind that is induced by the top and bottom surfaces can be obtained via thermal wind balance. The interior first baroclinic mean zonal wind is therefore approximately the difference between the NCEP data profile and the surface induced zonal wind. Figure 6 shows the NCEP averaged zonal wind with its mean subtracted (solid), the surface induced zonal wind (dash-dot), the residual first baroclinic wind (dotted) and the total zonal wind used in the model (dashed).

We chose model parameters as follows: latitude= 45°, $L = 10000km$, $H = 10km$, $N = 10^{-2}s^{-1}$, averaged NCEP long term mean values $U = 19.5m/s$, $\Theta_y^T = 4.34 \times 10^{-7}K/m$, $\Theta_y^B = -6.34 \times 10^{-6}K/m$ which for our model with sides of length 2π gives nondimensional model parameters $k_d = (L/2\pi)f/(NH) = 1.6$, $\beta = 2.1$ ($\check{\beta} = 0.48$), $r = 1$ ($\check{r} = 0.48$), $f = 1$, $H = 1$, $\Theta_y^T = 0.06$, $\Theta_y^B = -1.09$, and $\tilde{U}_1 = 0.17$. With these parameters the model produces the steady state spectra in figure 7, which transitions from -3 to $-5/3$ near model wavenumber $K \approx 50 - 100$ (wavelength 200-100km), although this scale may be sensitive to the value of Θ_y^T. Figure 8 shows that the dimensional flux of available potential energy at the top surface is $\epsilon \approx 3 \times 10^{-6}m^2s^{-3}$, which is less than the $\epsilon \approx 6 \times 10^{-5}m^2s^{-3}$ found in Cho and Lindborg (2001) on scales between $10km$ and $100km$ but is reasonable.

4. DISCUSSION

We have demonstrated that a balanced model that properly represents surface buoyancy dynamics will produce a

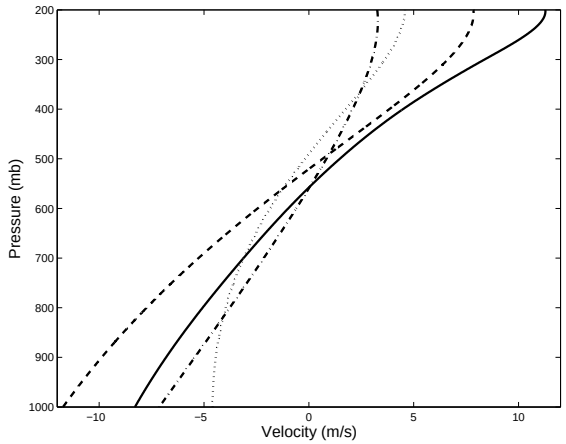

FIG. 6: Baroclinic NCEP zonal velocity averaged temporally, zonally and from 30°N to 60°N (solid); surface zonal wind profile inferred from Θ_y at 1000mb and 200mb (dash-dot); first baroclinic zonal wind when taken as the residual between the NCEP profile and the surface profile (dotted), and the sum of the surface and first baroclinic zonal winds which is the 2S2M approximation of the NCEP wind (dashed).

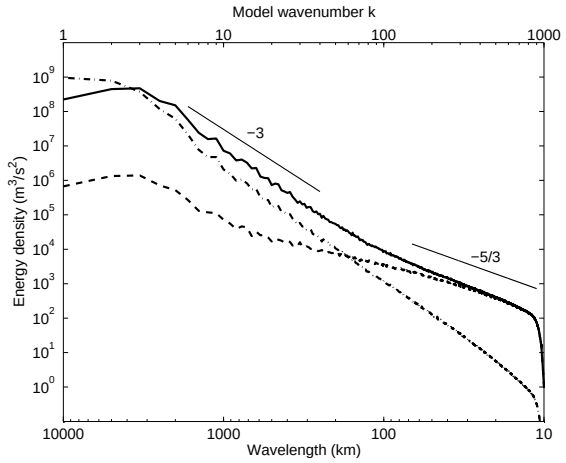

FIG. 7: The spectra using the atmospheric winds in figure 6. Shown are the kinetic energy at the top surface (solid), the barotropic kinetic energy (dash-dot), and the variance of potential temperature at the top surface (dashed).

robust forward cascade along its boundaries, with a spectrum that exhibits a shallowing from -3 to $-5/3$ slope, consistent with the observed atmospheric kinetic energy spectrum. The transition scale in this model is set by the ratio of the horizontal temperature gradients at the upper boundary and the interior; using midlatitude atmospheric parameters and mean gradients (at least as well as such can be represented in this truncated model) produces a

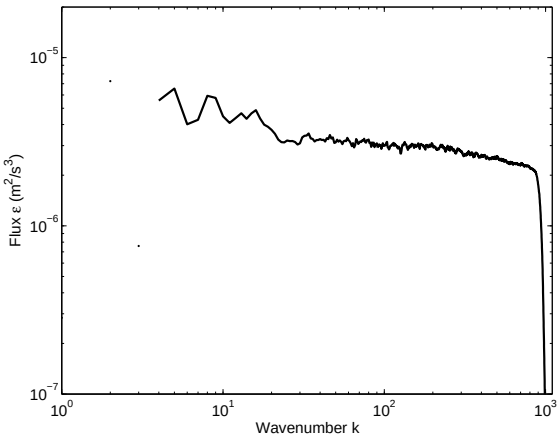

FIG. 8: The fluxes using the atmospheric winds in figure 6.

transition scale near the observed scale.

The proposed model is, of course, still incomplete. In particular it produces insufficient potential energy at large-scales — the GASP data shows potential and kinetic energy with nearly identical spectra at large and small scales, whereas the 2S2M model produces a weak APE spectrum at large scales (this may be the result of our severe truncation of vertical modes). Observations of the atmospheric energy spectra at mid-tropospheric depths are sparse, but those that do exist show a spectral slope of kinetic energy a little steeper than -2. The model proposed here, by contrast, produces an interior (mid-depth) spectrum with a slope with a minimum approaching -3.

REFERENCES

Blumen, W., 1978: Uniform potential vorticity flow: Part 1. theory of wave interactions and two-dimensional turbulence. *J. Atmos. Sci.*, **35**, 774–783.

Charney, J. G., 1971: Geostrophic turbulence. *J. Atmos. Sci.*, **28**, 1087–1095.

Cho, J. Y. N. and E. Lindborg, 2001: Horizontal velocity structure functions in the upper troposphere and lower stratosphere 1. observations. *J. Geophys. Res.*, **106**, 10223–10232.

Cho, J. Y. N., Y. Zhu, R. E. Newell, B. E. Anderson, J. D. Barrick, G. L. Gregory, G. W. Sachse, M. A. Carroll, and G. M. Albercook, 1999: Horizontal wavenumber spectra of winds, temperature, and trace gases during the pacific exploratory missions. Part I: Climatology. *J. Geophys. Res.*, **104**, 5697–5716.

Hakim, G. J., C. Snyder, and D. Muraki, 2002: A new surface model for cyclone-anticyclone asymmetry. *J. Atmos. Sci.*, **59**, 2405–2420.

Held, I. M., R. T. Pierrehumbert, S. T. Garner, and K. L. Swanson, 1995: Surface quasi-geostrophic dynamics. *J. Fluid. Mech.*, **282**, 1–20.

Juckes, M. N., 1994: Quasigeostrophic dynamics of the tropopause. *J. Atmos. Sci.*, **51**, 2756–2768.

Lapeyre, G. and P. Klein, 2006: Dynamics of the upper oceanic layers in terms of surface quasigeostrophy theory. *J. Phys. Oceanogr.*, **36**, 165–176.

Nastrom, G. D. and K. S. Gage, 1985: A climatology of atmospheric wavenumber spectra of wind and temperature observed by comercial aircraft. *J. Atmos. Sci.*, **42**, 950–960.

Tulloch, R. T. and K. S. Smith, 2006: A theory for the atmospheric energy spectrum: Depth-limited temperature anomalies at the tropopause. *Proc. Natl. Acad. Sci. U.S.A.*, **103**, 14690–14694.